Eur. Phys. J. C 13, 433–452 (2000)
Digital Object Identifier (DOI) 10.1007/s100520000314

THE EUROPEAN PHYSICAL JOURNAL C

Excess of continuum dimuon production at masses between threshold and the J/Ψ in S–W interactions at 200 GeV/c/nucleon

The HELIOS/3 Collaboration

A.L.S. Angelis[2,a], J. Antos[3], M. Beaulieu[4], H. Beker[2], J. Bystricky[8], M.-G. Catanesi[1], P. Cerello[9], S. Dagan[2,b], G. Dellacasa[9], S. Di Liberto[7], B. Dolgoshein[5], M. Esten[2,c], C. W. Fabjan[2], A. Gaidot[8], M. Gallio[1,d], P. Giubellino[9], U. Goerlach[2,e], C. Guerra[8], L.-A. Hamel[4], S. Konovalov[6], I. Kralik[3], G. London[8], F. Martelli[9,f], J.-P. Martin[4], M. Masera[9], M.-A. Mazzoni[7], F. Meddi[7], M.-T. Muciaccia[1], S. Muraviev[6], A. Nomerotsky[2], Y. Oren[2,g], J.-P. Pansart[8], G. Poulard[2], L. Ramello[9], L. Riccati[9], G. Rosa[7], L. Sandor[3], M. Sarris[2], E. Scomparin[9], A. Shmeleva[6], S. Simone[1], S. Smirnov[5], P. Taras[4], J. Urban[3], E. Vercellin[9]

[1] University of Bari and INFN, Bari, Italy
[2] CERN, CH-1211 Geneva, Switzerland
[3] Slovak Academy of Sciences, Košice, Slovak Republic
[4] University of Montreal, Montreal, Canada
[5] Lebedev Institute of Physics, Moscow, Russia
[6] Institute of Physics and Engineering, Moscow, Russia
[7] University of Rome "La Sapienza" and INFN Rome Italy
[8] DAPNIA, CE-Saclay, Gif/Yvette, France
[9] University of Turin and INFN Turin Italy

Received: 7 July 1999 / Revised version: 16 September 1999 /
Published online: 17 February 2000 – © Springer-Verlag 2000

Abstract. Results are presented on dimuon production for invariant masses ranging from the dimuon threshold up to the J/Ψ meson. Proton-tungsten and sulphur-tungsten interactions at 200 GeV/c/nucleon were measured over a large kinematic region, using the HELIOS/3 dimuon spectrometer at the CERN SPS. In the continuum regions between the dimuon threshold and the ρ/ω mesons, and between the ϕ and J/Ψ mesons, an excess is observed in S–W interactions relative to minimum bias p–W interactions. The observed excess is continuous over the explored mass range and has no apparent resonant structure. In the low mass region the dimuon yield increases by $(76 \pm 4)\%$ of the corresponding p–W dimuon spectrum, whereas in the higher mass region the excess amounts to 2.4 ± 0.3 times the p–W yield. The observed excess for the low mass region follows an exponential transverse mass distribution with an average inverse slope parameter T of (190 ± 5) MeV/c^2, constant for all but the lowest charged multiplicity interval and consistent with the slope of the excess in the higher mass region. In the invariant mass range of 1.35–2.5 GeV/c^2 the continuum dimuon mass distribution observed in p–W interactions can be quantitatively understood as a sum of three expected contributions (vector meson decays, semileptonic charm decays and Drell-Yan process), but both in central and in minimum bias S–W interactions an excess is observed with respect to these sources which does not depend on centrality, nor very strongly on the transverse momentum.

1 Introduction

Within the framework of QCD, a deconfinement phase transition from hadronic matter to quark matter, the Quark Gluon Plasma (QGP), should occur at high densities or high temperature. Various signals have been proposed to detect this new phase. Besides the well-studied effects of the deconfined QGP-phase on the formation on quarkonia states like the J/Ψ and the Υ, the hot plasma emits electromagnetic radiation, photons and lepton pairs.

[a] also McGill University, Montreal, Canada; now also at University of Athens
[b] also Saclay; on leave of absence from Tel Aviv University, Tel Aviv, Israel
[c] also University College, London, Great Britain
[d] now at University of Torino, Torino, Italy
[e] now at Institut de Recherches Subatomiques, UMR 7500, CNRS-IN2P3 et Université Louis Pasteur, Strasbourg, France
[f] now at University of Urbino, Urbino, Italy
[g] on leave of absence from Tel Aviv University, Tel Aviv, Israel

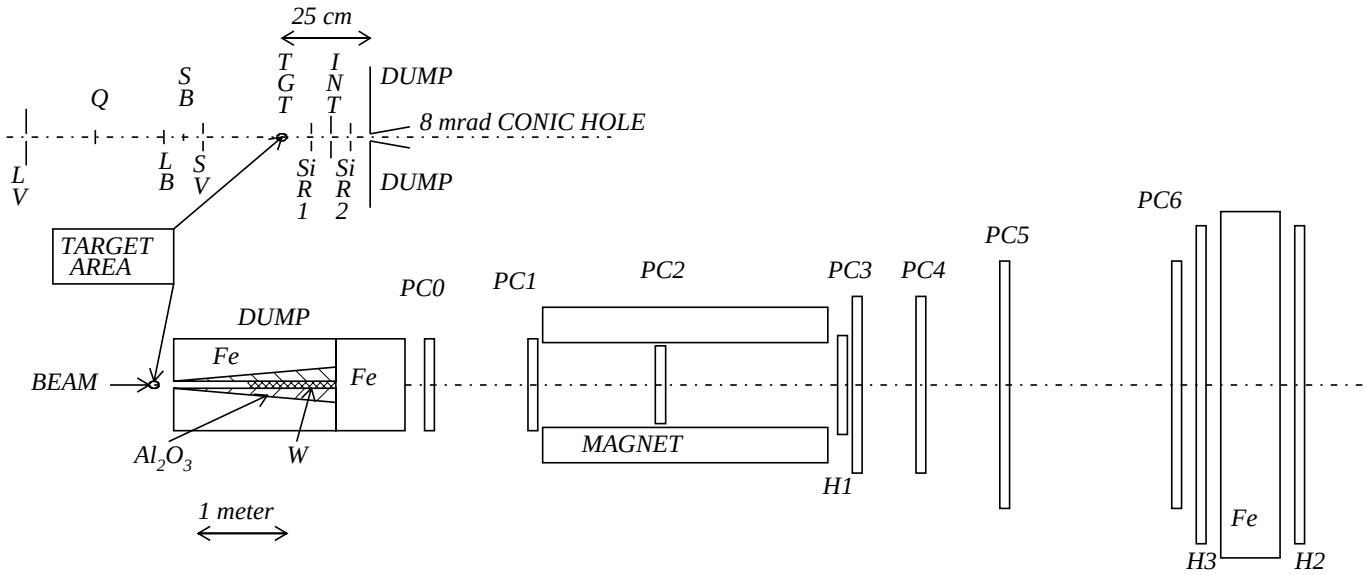

Fig. 1. Overall experimental setup with target region inset

Leptonic probes such as dimuons provide a direct way to study the radiation of the evolving QGP since leptons interact only electro-magnetically with the hadronic matter in which they are produced. Additional lepton pair-production is also expected from pion annihilation within the hot hadron gas or the mixed phase following the expansion of the quark gluon plasma. In the last years, much progress has been made in understanding the dynamics of the expanding matter and the processes in which dileptons and photons are emitted [1–3]. According to some calculations [4–8], a thermal dilepton signal might be expected in the mass region below the J/Ψ. Because of vector dominance the observed lepton spectrum should be strongly enhanced in the region of the ρ-mass [4,9–11]. However, in those phases of nuclear matter, such as the QGP, in which the ρ cannot exist as a bound state due to chiral symmetry restoration [12], this enhancement at the ρ resonance is suppressed. In-medium effects in nuclear matter can further shift the effective mass and alter the width of the ρ resonance as discussed in [13–17].

The HELIOS/3 experiment operated at the CERN SPS with 200 GeV/c/nucleon beams. The experiment studied p–W and S–W collisions and was designed mainly to measure low transverse mass dimuons ($m_T = \sqrt{m^2 + p_T^2}$: low masses, low transverse momenta) and vector mesons ρ, ω, ϕ in a wide kinematic region. The number of dimuons in the "intermediate mass" region (i.e. masses between the ϕ and J/Ψ or 1.35-2.5 GeV/c^2) was found to be reasonably large to search also in this region for a possible new dimuon source.

This paper presents the data of the dimuon spectrum in the mass region from threshold to the J/Ψ meson, and discusses the continuum data below the ρ meson (below 0.7 GeV/c^2, "low mass region") and in the intermediate mass region. The mesons themselves (ρ, ω, ϕ and J/Ψ) have been the subject of a separate paper [18]. The multiplicity of charged hadrons accompanying the dimuons was used as a measure of the collision centrality.

We first briefly recall the experimental set-up and the important aspects of the analysis described in detail elsewhere [18], and then present the experimental results on the dimuon yield, normalized to the charged particle production within a similar pseudo-rapidity region. Our analysis of these results consists of two different approaches: (1) a purely experimental one in which we compare directly the p–W and S–W spectra and (2) a detailed comparison of the continuum results in the intermediate mass region with the known sources of dimuon production in hadron-hadron interactions [19].

It should be pointed out that early indications of an excess in S–W interactions measured in HELIOS/3 in the intermediate mass region have already been reported [20–22]. Similar findings were reported by the NA38/NA50 collaboration in the intermediate mass region [23] and by the CERES collaboration in the low mass region [24]. It should be emphasized that this paper covers both mass regions, thus allowing an investigation of a possible common physical interpretation.

2 Experimental set-up and trigger

The experimental configuration is shown in Fig. 1. The z-axis of our right-handed coordinate system with its origin at the target position coincides with the beam direction, while the y-axis is oriented vertically. The target region with beam counters, silicon ring counters (SR1, SR2) and a scintillator petal hodoscope (INT), used to signal the interaction, is detailed in the inset.

The sulphur beam was identified using information from scintillator and quartz counters; a Čerenkov counter was used for the proton run.

A 5 or 10 mm long tungsten wire of 1.0 mm diameter oriented parallel to the beam served as a target, corresponding to 13% or 12% interaction lengths calculated using the inelastic S–W or p–W cross sections, respectively. The charged particle multiplicity was measured by two silicon ring counters (covering the overlapping pseudorapidity regions $1.6 \leq \eta \leq 3.7$ and $2.6 \leq \eta \leq 5.5$). The dimuon spectrometer consisted of a hadron absorber, six interaction lengths of Al_2O_3 and 100 cm of Fe, followed by a magnetic spectrometer and muon hodoscopes. The absorber was carefully optimized for the measurement of low m_T pairs, and placed only 25 cm downstream from the target in order to minimize the background of decay muons. Except for the addition of the first scintillator hodoscope H1 consisting of fourteen 2×0.15 m^2 slabs, the configuration of the spectrometer was identical to the one used in the HELIOS/1 experiment [25]. The acceptance of the spectrometer was similar to the subset of the silicon ring counters used in the charged multiplicity trigger, $3.7 < \eta < 5.5$.

With and without the requirement of two muon candidates in the muon spectrometer, three discrimination levels on the charged multiplicity were used at the trigger level to enhance the number of central events; the levels correspond to the beginning of the plateau, the knee and the tail of the multiplicity distribution [26] in order to cover the range between peripheral and central collisions. In addition, events flagged only by the interaction trigger signal and validated by the pile-up protection were accepted. No multiplicity signal from the silicon detectors was required for these events. They correspond to very low multiplicities, subsequently referred to as the minimum bias sample.

3 Analysis

3.1 Data reduction

During data taking with the 200 GeV/c sulphur beam on the tungsten target, 9×10^6 dimuon triggers were taken. This number was reduced by applying off-line criteria briefly recalled here and described in [18].

The information from various beam detectors was used off-line to reject events associated to a non-sulphur projectile, and pile-up events as well. The rejection of the contamination due to interactions outside the target was based on the information from the two ring multiplicity detectors.

The muon reconstruction was done using a standard procedure of point-track association and reconstruction. For successfully reconstructed tracks, an overall minimum χ^2 probability of 1% was required. Requiring at least 2 reconstructed tracks reduces the event sample to about 40% of the original number. The correspondence of an H2/H3 coincidence with a charged track defines a muon. The requirement that exactly 2 muons are identified reduces the number of events by about a factor 10. This is largely due to the fact that the chamber wires used in the trigger were orthogonal to the muon-hodoscope slabs.

To suppress events with dimuons produced by the secondary particles in the absorber, reconstructed muon tracks had to point to the target. The definition of this cut took into account the uncertainty and the apparent shift of the reconstructed production vertex due to multiple scattering. This phenomenon is well understood and reproduced in simulation programs. For each muon track, Z, the point of the closest approach to the beam axis, relative to the target, was calculated together with its error σ_Z. Only tracks with $Z < 250$ cm and $Z/\sigma_Z < 3$ were accepted.

The muon momentum reconstructed behind the hadron absorber had to be corrected for the average energy loss and the multiple scattering. The energy loss correction was modeled by a GEANT simulation. The muon polar angle was calculated by combining the angle measured in the spectrometer with an uncorrelated estimate which required that the track originated in the target as described in [18]. The reconstruction method was verified for the ϕ and J/Ψ mesons. The mass resolution at these masses, 82 and 90 MeV/c^2, respectively, agreed with our GEANT simulation.

After all cuts were applied, there remained 2.7×10^5 dimuon events in the sulphur run, of which 68.4% were $\mu^+\mu^-$, 14.4% $\mu^+\mu^+$ and 17.2% $\mu^-\mu^-$. Similar selection resulted in 44200 dimuon events for the proton beam run with 95.6% $\mu^+\mu^-$, 3.3% $\mu^+\mu^+$ and 1.1% $\mu^-\mu^-$. In the 1.35-2.5 GeV/c^2 mass region, the corresponding numbers were 8500 dimuons in the sulphur run, of which 57.3% were $\mu^+\mu^-$, 23.3% $\mu^+\mu^+$ and 19.4% $\mu^-\mu^-$ and, for protons, 339 dimuons with 285 $\mu^+\mu^-$, 45 $\mu^+\mu^+$ and 9 $\mu^-\mu^-$.

In most events only two muons were reconstructed. The percentage of 3 or more identified muons was about 7% in the sulphur sample, and less in the proton sample.

The acceptance was calculated on a $19 \times 17 \times 13$ grid of mass m, transverse momentum p_T, and laboratory rapidity y using a full GEANT simulation of the detector. [1] To reject events with very low acceptance while retaining a maximal kinematic region for the analysis, we defined the cuts as:

$$m_T \geq 4(7 - 2y)$$
$$m_T \geq \sqrt{(2m_\mu)^2 + \left(\frac{2P_{min}}{\cosh y}\right)^2} \quad (1)$$

where y is the dimuon rapidity and P_{min}=7.5 GeV/c is larger than the minimum momentum necessary to traverse the spectrometer due to the energy loss in the absorber and the strength of the magnetic field. For example, in Fig. 5 of [18], we show the ρ acceptance in the y vs m_T

[1] The decay angular distribution of the dimuon was assumed to be isotropic. This is consistent with the results of [25]. For dimuons from charm decay, the distribution depends on the mass of the dimuon[19]. The implications of these different distributions will be discussed in Sect. 5.

plane. To investigate a possible dependence of dimuon production on the transverse momentum and rapidity, the accepted kinematic region (1) was divided into the following subregions

$$\begin{aligned} y &< 3.9 \\ 3.9 \leq y &< 4.4 \\ y &\geq 4.4 \\ p_T &< 0.35 \text{ GeV}/c \\ 0.35 \leq p_T &< 0.6 \text{ GeV}/c \\ p_T &\geq 0.6 \text{ GeV}/c \end{aligned} \quad (2)$$

Note that, as will be explained subsequently, the rapidity interval above $y > 4.4$ is not fully used in our continuum analysis, due to uncertainties at very forward rapidity of the remaining background at very low masses and due to the lack of statistics in the higher mass region.

3.2 Multiplicity classes

The multiplicity of charged particles was measured in the pseudo-rapidity region $3.5 < \eta < 5.2$ and carefully corrected for secondary interactions, mainly electron pair production in the target as described in [18]. It was used to group our S–W data according to their multiplicity into six classes, requiring that the trigger samples contributing to each class gave comparable average multiplicities. In addition, three other classes were defined using the fractions determined from the interaction trigger with no muon requirement: a special class of events, subsequently referred to as the "minimum bias" class, was constructed from all multiplicity classes, a second class containing predominantly peripheral collisions was constructed from the multiplicity classes 2–3, and a class of central collisions was based on multiplicity classes 4–6. For the second analysis of this paper concerning the intermediate mass region, only the minimum bias class and individual classes 3–6 were used since the statistics in the classes 1–2 were not sufficient for a detailed analysis in this mass region.

Table 1 contains the number of projectile participants estimated for each multiplicity class using the Monte Carlo code VENUS 3.11 [27]. We emphasize that the impact parameter distributions corresponding to the more central multiplicity classes have significant overlap with those contributing to other multiplicity classes. This feature was cross-checked using a different version (VENUS 4.12) [28] of the program and further by the DTUNUC 1.02 model [29] and the FRITIOF [30] code. All give qualitatively similar results although the numerical values for the deduced range of impact parameters can differ by about one fermi. This is important when specific models are used to evaluate the yield of dimuon production. In that case, it is of greater advantage to choose the generator which describes best the experimental multiplicity distributions, see the discussion in Sect. 4.2.2.

The mean multiplicity in the p–W data was 4.6 with an RMS = 2.5.

3.3 Normalization to charged particle production

Together with the dimuon triggers, events with no muon requirement but the same multiplicity thresholds were also acquired. These events were used for the normalization of the dimuon yield to the number of charged particles in each multiplicity class. The $\mu\mu/charged$ ratios were calculated at the trigger level, so that the multiplicity trigger acceptances canceled. The various trigger contributions to each multiplicity class were then combined using the statistical error for each trigger to weigh its contribution [18].

3.4 Combinatorial background

An important background for any dimuon continuum analysis in events with a high charged particle multiplicity is that due to uncorrelated muon pairs originating from π, K or other meson decays which are measured in the same event as a dimuon. If we suppose that all like-sign muon pairs were of this kind, the combinatorial background in the unlike-sign samples, N_c^{+-}, is proportional to the geometric mean of the like-sign samples with the proportionality constant defined as:

$$R \equiv N_c^{+-}/2\sqrt{N^{++}N^{--}} \quad (3)$$

The constant R was studied extensively by a full Monte Carlo simulation [31], using the VENUS 3.11 event generator to produce events in which particles with short lifetimes (e.g. K_S) decay. The decay probability of each charged π and K meson (produced directly or via decay) was calculated, assuming a potential decay path equal to the distance between the target and the absorber front face plus one interaction length in the absorber. The mesons were forced to decay within this decay path and the resulting muons were tracked through the apparatus using a GEANT 3.14 based program. Muons within the spectrometer acceptance were combined in all possible ways to give pairs. Those pairs satisfying the hodoscope trigger were then weighted with the appropriate decay probabilities and used to calculate $R = 1.14 \pm 0.02$ for the sulphur runs in all multiplicity classes and 1.57 ± 0.10 for the proton runs. The R-value for sulphur interactions does not show a significant dependence on charged multiplicity class (since even the lowest class has a relatively high multiplicity relative to p–W interactions) nor on mass or transverse mass.

Detailed comparisons were made between the data and the Monte Carlo simulation, in particular the 1μ and 2μ distributions; the results were quite similar. The comparison with the Monte Carlo prediction of the absolute value of the like-sign data relative to the number of charged particles grouped in the multiplicity classes, is relatively satisfactory: the multiplicity dependence is similar in data and in simulation, and the naively expected squared-multiplicity dependence is reached at high masses.

To obtain a precise shape of the combinatorial background, reducing the bin-to-bin statistical errors, we used muon pairs formed by muons of different like-sign events

Table 1. Charged multiplicity classes in S–W interactions evaluated using the VENUS 3.11 program

Class	Multiplicity in $3.5 < \eta < 5.2$	$\langle MULT \rangle$	projectile participants	impact parameter (fm)
			Average (RMS)	
1	$MULT \leq 25$	14.0	3.7 (3.0)	10.0 (1.4)
2	$25 < MULT \leq 70$	43.5	14.5 (5.6)	7.3 (1.2)
3	$70 < MULT \leq 100$	80.8	22.7 (5.5)	5.6 (1.5)
4	$100 < MULT \leq 130$	115.8	26.6 (4.8)	4.3 (1.7)
5	$130 < MULT \leq 160$	147.0	29.4 (2.6)	3.5 (1.5)
6	$160 < MULT$	165.1	30.6 (1.7)	2.9 (1.3)
minimum bias		67.7	16.7 (4.2)	6.8 (1.4)
periph. coll.	$25 < MULT \leq 100$	54.1	16.8 (5.6)	6.8 (1.3)
central coll.	$100 < MULT$	134.6	28.2 (3.5)	3.8 (1.6)

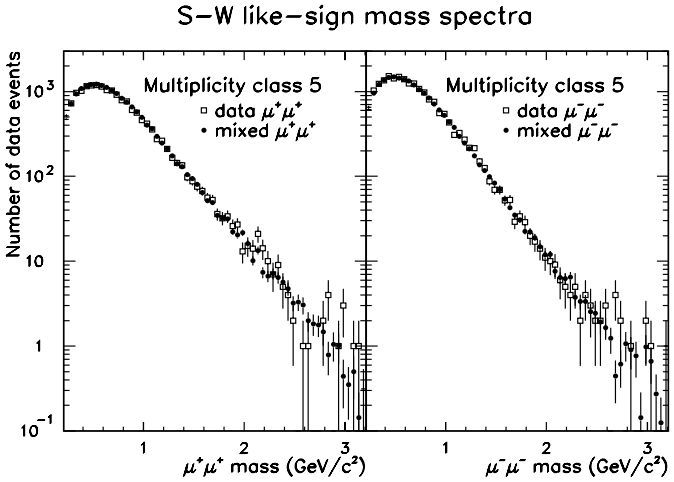

Fig. 2. Comparison of mixed like-sign events with real like-sign events for one of the classes. The event samples are relatively normalized

belonging to the same multiplicity class [32]. The trigger requiring two hits in the H2/H3 coincidence rejected dimuons with both muons in the same slab of H2/H3. The probability to detect a muon in a slab was estimated from the accepted dimuons in each multiplicity class separately for $\mu^+\mu^+$ and $\mu^-\mu^-$. A weight was attributed to each muon to remove the trigger bias. Dimuons of all sign combinations were then randomly formed and only pairs meeting the trigger conditions were accepted. In this procedure the same muon was used between 10 to 50 times to form uncorrelated unlike-sign muon pairs. A check of the method was made by comparing the dimuon mass, transverse momentum and rapidity distributions for the mixed like-sign sample with those of the measured like-sign sample; this leads to a χ^2/degree of freedom = 1608/1579 = 1.02, combining the p–W and S–W data.

An example of the good precision of the method over the entire mass range is demonstrated in Fig. 2 where the real and mixed like-sign mass spectra are shown together for multiplicity class five. The overall normalization for the mixed unlike-sign combinatorial background was given by the number of real like-sign events via equation (3). The statistical errors of the mixed dimuon spectra, including correlations due to the repeated use of the same muon, are negligible with respect to the error of the constant R.

Note that the shape of the combinatorial background is such that a higher normalization constant R would lead, after subtraction of the combinatorial background from the measured unlike-sign data, to some large negative bins incompatible with the errors.

3.5 Absorber background

Another important background present in low transverse mass dimuon measurements is that produced by interactions of produced hadrons or of sulphur projectile fragments in the absorber. A large part of this background is rejected by the target cut.

We estimated the spectral shape and absolute rate of the remaining background with the results of special runs with π beams of 25, 50 and 100 GeV/c impinging on the absorber front face, and 200 GeV/c protons impinging on the absorber W plug, and used a physics generator for interpolation [33].

In these runs, we weighted the accepted dimuons with the reconstruction efficiency, subtracted the combinatorial background, and obtained mass, transverse momentum, rapidity and Z distributions which were normalized per incoming particle interacting in the absorber. The latter required a small subtraction of the beam muons.

In the generator, the production of charged hadrons used the $dN^{charged}/d\eta$ distribution as measured by the HELIOS/2 experiment [26], and an exponential p_T distribution with an average value of 0.365 GeV/c. The latter is modulated by a y-dependent Gaussian centered at the p–p center of mass rapidity with a width of 3 units. The resulting hadron was tracked in GEANT until its interaction in the absorber, and its momentum determined the

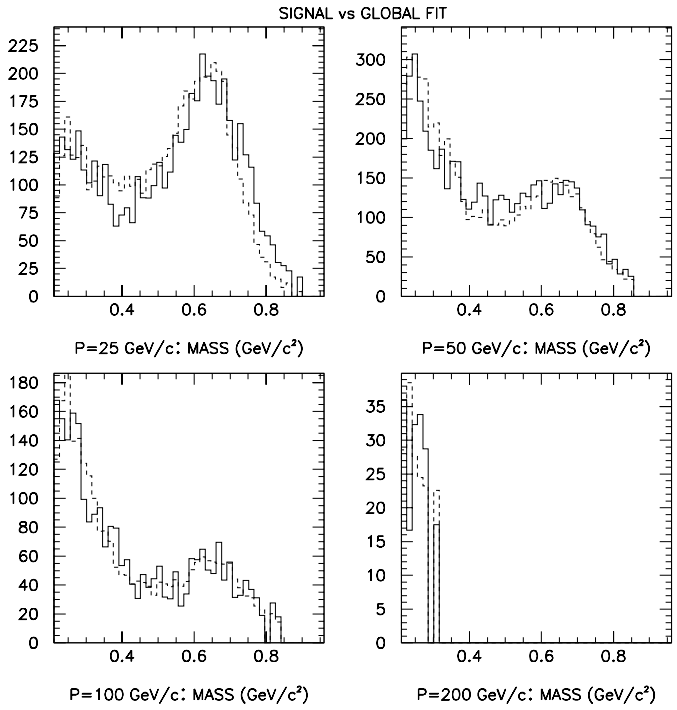

Fig. 3. Comparison of mass spectra between data (solid histogram) and the fitted mass-distributions used for the background subtraction (dashed histogram). The histograms are normalized to each other

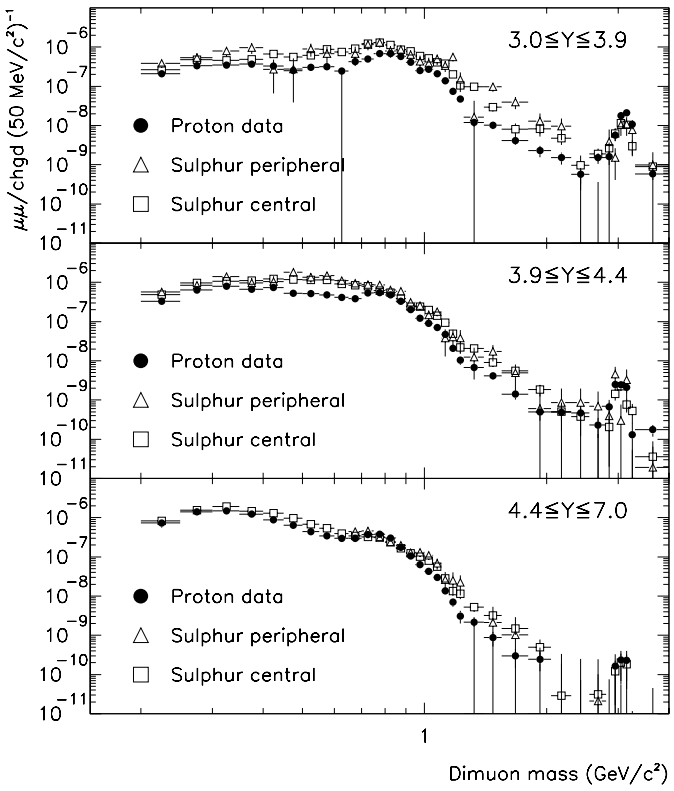

Fig. 4. The ratio $\mu\mu$ /(charged multiplicity) vs. mass in three different rapidity intervals for p–W minimum bias interactions, S–W peripheral interactions and S–W central interactions. The charged multiplicity is measured in the pseudorapidity interval of 3.5–5.2

meson mix of $\eta, \rho, \omega, \eta'$ and ϕ. The resulting $\mu\mu$ spectra were composed of a sum of two- and three-body decays of these mesons. The p_T and x_F distributions were taken from [34] in which πC and pC interactions at 150 GeV/c and 225 GeV/c were studied. The pC measurements were rescaled to heavier target nuclei to describe the interaction with the W plug. As in the acceptance calculation, the decay angular distribution of the dimuon was assumed to be isotropic. The muons were then tracked through the apparatus. For each of the four beam momenta, we produced five data sets corresponding to the 5 resonances and their branching ratios.

The relative production probabilities of the mesons were determined at each momentum by a fit to the mass spectrum. In principle, these fractions are unique at a given momentum, but vary as a function of momentum. In order to be able to interpolate, the momentum dependence for the fraction of each resonance was fit to a quadratic function of momentum. The $\eta, \rho, \omega, \eta'$ and ϕ fractions at 200 GeV/c were fixed at 0.444, 0.084, 0.392, 0.062, 0.018, respectively [25]. Since the amounts of η' and ϕ were not well-constrained, the ratios η'/ρ and ϕ/ρ were fixed at their measured values at 200 GeV/c.

The p_T and rapidity distributions required only a small adjustment in shape and momentum dependence. The absolute normalization for the Monte Carlo was determined at each of the four momenta, and was fit to a quadratic function of momentum. The final fit involved the normalized m, p_T, y, Z and Z/σ_Z spectra, as well as the absolute normalization, with 559 degrees of freedom (DOF).

The results of the comparison of the data with the fit to the mass spectra are shown in Fig. 3.

Though the fit gives the general trend of the data, the confidence level is very poor. The point-to-point relative errors for the predictions were increased by adding a term in quadrature to take into account systematic uncertainties. To obtain a confidence level between 1% and 99%, the additional relative error varied between 12% and 20%. We chose to use 15%, roughly the value for $\chi^2/\mathrm{DOF} = 1$.

In the case of sulphur projectiles, an extra background is produced by non-interacting projectile nucleons ("fragments"). The mean atomic weight of the fragments, $\equiv$ A, depends on the multiplicity class. For this background, we have used the fits to the special proton run distributions, multiplied by $A^{2/3}$ [35].

Note that the reconstruction algorithm imposes the dimuon vertex to coincide with the target position and therefore shifts the effective mass and transverse momentum of dimuons produced in the absorber towards lower values, and the effective rapidity to higher values.

In the intermediate mass region, the absorber background plays a negligible role, however it limits the low mass region at high y, in particular at low multiplicity where the fragment production is most important and due to the discussed uncertainties possibly inadequately modeled.

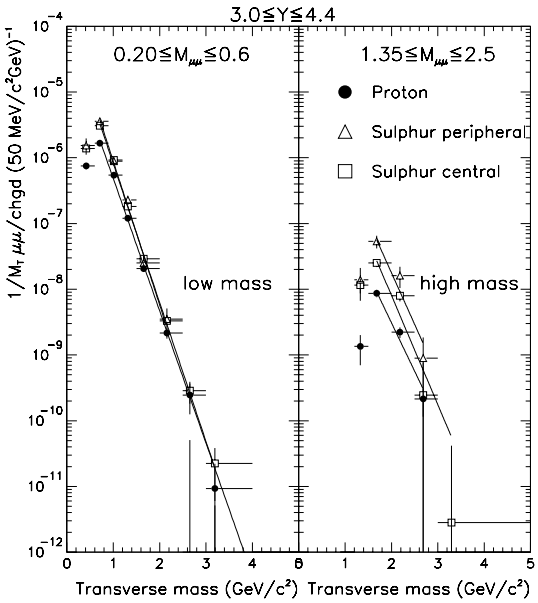

Fig. 5. The ratio $\mu\mu$/(charged multiplicity) vs. transverse mass for low and high mass regions for p–W minimum bias interactions, S–W peripheral interactions and S–W central interactions. The ratio is divided by M_T to obtain an exponential distribution

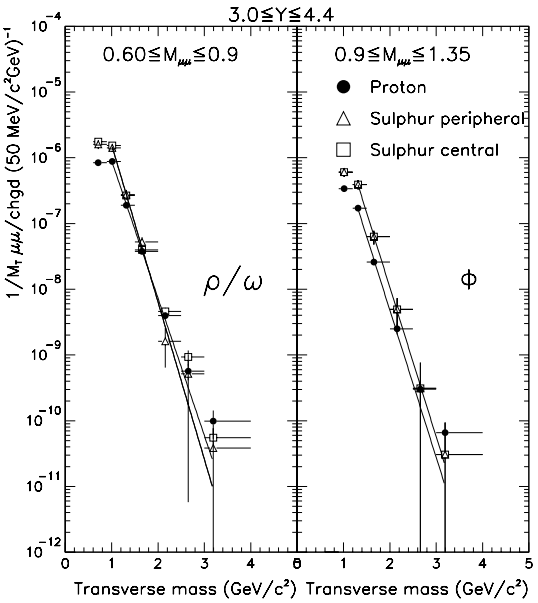

Fig. 6. The ratio $\mu\mu$/(charged multiplicity) vs. transverse mass for $\rho - \omega$ and ϕ mass regions for p–W minimum bias interactions, S–W peripheral interactions and S–W central interactions. The ratio is divided by M_T to obtain an exponential distribution

4 Results

The experimental results are expressed by the quantity $\mu\mu$/(charged multiplicity) which is given by the ratio of the number of dimuons in a mass and rapidity interval within the acceptance defined by expressions (1) and (2) divided by the number of charged particles measured in the interval of $3.5 < \eta < 5.2$, given by the multiplicity in the Silicon detectors. These ratios are presented as a function of mass for a given rapidity region. For reasons of statistical significance, we have adjusted the binning to the low counting rate at higher masses. In Tables 2–4 and Fig. 4, we give the experimental results on dimuons for p–W minimum bias interactions, S–W peripheral interactions and S–W central interactions in three different rapidity intervals, ranging from 3 to 7. The data for low mass ($m_{\mu\mu} < 0.65$ GeV/c^2) pairs in S–W peripheral interactions are only shown for rapidities below 4.4 due to the remaining uncertainty in the absorber background subtraction at large rapidities.

Assuming that the yield of muon pairs is dominated by the decays of meson resonances in the low mass region, it will scale with the charged particle multiplicity [25]. Any additional dimuon source would lead to increased values of the dimuon to charged particle ratio measured relative to some reference. As such a reference, one could choose either a Monte Carlo simulation taking into account all known contributions and their dependence on rapidity and transverse mass convoluted with the acceptance of our spectrometer or our measured dilepton spectra of p–W interactions where a priori no new source of dilepton pairs is expected. We choose the second possibility as we have not, up to now, found a fully satisfactory reproduction of our proton tungsten data by any simulation program.

In the intermediate mass region the most dominant dilepton sources in proton nucleus collisions are Drell Yan and open charm production, which scale differently with the charged particle multiplicities. However, our choice of the dimuon normalization was motivated by the fact that all models for enhanced dilepton production involve a stronger than linear dependence on the charged multiplicity.

4.1 Direct comparison of S–W and p–W data

In our first analysis, we choose our proton tungsten data as the reference to which we compare the sulphur data.

Figure 4 shows the mass spectra for p–W, S–W peripheral and S–W central interactions. The overall shape of the dimuon mass distribution changes with rapidity due to the rapidity dependent m_T cut-off of the spectrometer acceptance given by equation (1). We note that in the mass region up to the J/Ψ resonance, the S–W data are above the p–W data. The suppression of the J/Ψ resonance is apparent in the S–W data. Figures 5 and 6 show the transverse mass spectra in four different mass regions. Together with a fit to the function $dN/dM_T^2 = Ae^{-M_T/T}$ characterized by the inverse slope parameter T, summarized in Fig. 7. The centroid within each m_T bin has been re-calculated taking into account the exponential slope of the distribution. The effect of this correction on the absolute values of the inverse slope parameters varies by 5 and 10 MeV for the low and high mass regions, respectively. We note that the inverse slopes in the different mass re-

Table 2. The $\mu\mu$/(charged multiplicity) ratio ($\equiv$ number of dimuons in the given mass and rapidity interval integrated over p_T normalized to the charged particles measured in $3.5 < \eta < 5.2$) for rapidities $3.0 \leq y(m_{\mu\mu}) \leq 3.9$. Note the variable mass bins. The results in the first bin are affected by the dimuon threshold

Mass interval (GeV/c^2)	p–W	S–W (periph. coll.)	S–W (central coll.)
	$10^9 \times (\mu\mu/0.05\ \mathrm{GeV}/c^2)$ per charged particle		
	$3.0 \leq y(m_{\mu\mu}) \leq 3.9$		
0.20-0.25	210.±19.	389.±93.	267.±24.
0.25-0.30	336.±39.	535.± 156.	477.±43.
0.30-0.35	349.±47.	790.± 221.	458.±58.
0.35-0.40	371.±38.	961.± 292.	489.±64.
0.40-0.45	328.±35.	272.± 206.	672.±74.
0.45-0.50	252.±32.	277.± 238.	555.±76.
0.50-0.55	307.±37.	901.± 336.	612.±88.
0.55-0.60	319.±40.	679.± 340.	884.±96.
0.60-0.65	244.±43.	0.0± 278.	757.±95.
0.65-0.70	424.±45.	678.± 348.	913.±98.
0.70-0.75	500.±42.	1161.± 335.	1233.±98.
0.75-0.80	684.±47.	1306.± 332.	1305.±91.
0.80-0.85	680.±42.	792.± 258.	1134.±82.
0.85-0.90	578.±36.	858.± 236.	863.±72.
0.90-0.95	407.±31.	636.± 179.	778.±63.
0.95-1.00	252.±22.	435.± 167.	598.±53.
1.00-1.05	269.±21.	386.± 157.	515.±44.
1.05-1.10	209.±19.	494.± 145.	407.±38.
1.10-1.15	139.±15.	335.± 104.	377.±33.
1.15-1.20	75.±11.	563.± 132.	203.±27.
1.20-1.25	47.2±8.2	149.±77.	105.±22.
1.25-1.40	11.9±2.6	16.4±27.	97.±11.
1.40-1.55	10.2±2.0	98.3±26.	29.3±6.7
1.55-1.80	4.2±.98	39.7±14.	8.1±3.2
1.80-2.05	2.3±.73	12.8±7.6	8.2±2.0
2.05-2.30	1.5±.52	9.6±5.4	4.7±1.6
2.30-2.55	0.6±.26	0.0±0.5	1.0±0.7
2.55-2.80	1.5±.46	0.0±0.4	1.9±0.7
2.80-2.90	1.6±.64	3.8±4.0	2.6±1.0
2.90-3.00	5.6±1.6	1.5±1.1	6.3±2.2
3.00-3.10	17.7±2.5	10.4±4.9	11.6±1.9
3.10-3.20	21.1±2.9	10.9±5.5	10.4±1.8
3.20-3.30	10.9±2.9	7.7±6.0	3.0±1.2
3.30-4.00	0.6±.18	1.0±1.1	0.9±0.3
4.00-5.00	0.0±.03	0.0±0.0	0.1±0.1

gions are consistent within 10% with p–W, and peripheral and central S–W collisions, except in the ρ/ω region where the m_T distribution in p–W is characterized by a 15% larger inverse slope parameter.

We form the difference between the $\mu\mu$/(charged multiplicity) in S–W and p–W minimum bias interactions; a significant non-zero difference could indicate a possible signal for new physics in S–W interactions.

The difference in S–W central and peripheral interactions is plotted as a function of mass in Fig. 8 where the overall rapidity interval is also subdivided into three. The excess is clearly statistically significant. Except for the $\rho/\omega/\phi$-resonance region where the enhancement of the ϕ plays a role [18], the mass spectra of the dimuon excess are continuous from very small to large values. The turnover at low mass is due to acceptance cuts. The shape and ab-

Table 3. The $\mu\mu$/(charged multiplicity) ratio as defined in Table 2 but for rapidities $3.9 \leq y(m_{\mu\mu}) \leq 4.4$

Mass interval (GeV/c^2)	p–W	S–W (periph. coll.)	S–W (central coll.)
	$10^9 \times (\mu\mu/0.05\ \mathrm{GeV}/c^2)$ per charged particle		
	$3.9 \leq y(m_{\mu\mu}) \leq 4.4$		
0.20-0.25	327.±44.	564.±119.	486.±30.
0.25-0.30	647.±81.	843.±190.	972.±60.
0.30-0.35	798.±70.	1399.±340.	1072.±76.
0.35-0.40	671.±77.	959.±351.	1111.±93.
0.40-0.45	731.±57.	1049.±383.	1219.±102.
0.45-0.50	527.±47.	1802.±404.	1184.±101.
0.50-0.55	521.±45.	1353.±361.	1162.±93.
0.55-0.60	481.±38.	1492.±316.	1154.±79.
0.60-0.65	418.±36.	1112.±233.	908.±61.
0.65-0.70	387.±31.	945.±174.	844.±49.
0.70-0.75	542.±27.	876.±142.	796.±39.
0.75-0.80	546.±23.	867.±126.	617.±31.
0.80-0.85	475.±19.	640.±95.	550.±26.
0.85-0.90	329.±15.	590.±91.	384.±22.
0.90-0.95	203.±12.	308.±65.	240.±17.
0.95-1.00	121.±8.5	254.±54.	240.±15.
1.00-1.05	91.±7.2	146.±44.	198.±13.
1.05-1.10	71.0±6.2	178.±42.	140.±11.
1.10-1.15	46.8±5.1	38.0±25.	94.3±9.3
1.15-1.20	20.5±3.6	40.3±21.	49.4±7.4
1.20-1.25	10.4±2.4	37.8±23.	21.7±5.9
1.25-1.40	6.8±1.1	12.4±9.1	20.7±2.9
1.40-1.55	4.1±.85	17.3±7.8	9.1±2.0
1.55-1.80	1.4±.36	4.9±3.2	5.5±1.0
1.80-2.05	0.5±.20	0.6±1.6	1.8±.61
2.05-2.30	0.5±.19	0.9±1.1	0.5±.35
2.30-2.55	0.5±.18	0.9±1.1	0.4±.26
2.55-2.80	0.2±.12	0.7±.96	0.0±.13
2.80-2.90	0.7±.35	0.4±.47	0.2±.18
2.90-3.00	2.5±.66	4.5±2.5	1.4±.45
3.00-3.10	2.4±.62	0.3±.46	2.3±.57
3.10-3.20	2.1±.55	3.2±2.7	0.8±.29
3.20-3.30	0.1±.13	0.0±.05	0.5±.27
3.30-4.00	0.2±.06	0.0±.07	0.0±.03
4.00-5.00	0.0±.00	0.2±.21	0.0±.02

solute size of the excess in our peripheral and central data samples are nearly identical within our statistical and systematic errors except for a weak tendency for a somewhat larger excess in the higher mass region for peripheral collisions.

To investigate further the dependence on centrality, Fig. 9 shows the integrated excess in two mass regions, 0.2–0.6 GeV/c^2 and 1.35-2.4 GeV/c^2, respectively, as a function of the charged multiplicity. In this figure the observed dimuon excess has been normalized to the dimuon production in p–W collisions in order to give an indication of its strength relative to p–W. The overall rapidity interval is divided in three. The average values for the excess in the two mass regions and the three rapidity intervals are listed in Table 5.

Whereas the low mass interval exhibits an additional contribution of (0.76 ± 0.04) times the p–W sources for $3.0 \leq y \leq 4.4$, independent of multiplicity within 10% falling to (0.26±0.05) at very forward rapidities, the higher mass region is on average a factor of 2.4 ± 0.3 higher for all rapidities. The weak indication (at the 2 sigma level) for the higher mass region to decrease with centrality in

Table 4. The $\mu\mu$/(charged multiplicity) ratio as defined in Table 2 but for rapidities $4.4 \leq y(m_{\mu\mu}) \leq 7.0$. For this rapidity interval, the low mass pairs ($m_{\mu\mu} < 0.65$ GeV/c^2) of the peripheral collisions are affected by the remaining uncertainty of the absorber background correction and are therefore excluded from the table

Mass interval (GeV/c^2)	p–W	S–W (periph. coll.)	S–W (central coll.)
	$10^9 \times (\mu\mu/0.05$ GeV/$c^2)$ per charged particle		
	$4.4 \leq y(m_{\mu\mu}) \leq 7.0$		
0.20-0.25	732.±174.	–	834.±121.
0.25-0.30	1416.±224.	–	1560.±167.
0.30-0.35	1488.±147.	–	1936.±127.
0.35-0.40	1212.±94.	–	1472.±102.
0.40-0.45	875.±54.	–	1293.±73.
0.45-0.50	639.±32.	–	959.±49.
0.50-0.55	441.±23.	–	675.±35.
0.55-0.60	341.±18.	–	542.±27.
0.60-0.65	296.±15.	–	389.±21.
0.65-0.70	296.±15.	444.±73.	344.±18.
0.70-0.75	371.±14.	463.±67.	325.±16.
0.75-0.80	379.±13.	311.±51.	320.±14.
0.80-0.85	301.±12.	234.±43.	241.±12.
0.85-0.90	174.±8.6	198.±39.	164.±9.7
0.90-0.95	106.±6.6	129.±31.	124.±8.2
0.95-1.00	62.9±5.1	131.±31.	101.±7.2
1.00-1.05	42.5±4.1	109.±26.	79.7±6.4
1.05-1.10	29.9±3.4	68.5±22.	56.3±5.3
1.10-1.15	13.6±2.3	26.2±15.	28.5±4.0
1.15-1.20	7.0±1.7	25.4±15.	13.5±3.2
1.20-1.25	3.1±1.1	22.2±12.	11.4±3.1
1.25-1.40	2.2±.54	0.0±2.9	5.2±1.2
1.40-1.55	0.9±.36	2.1±3.2	3.2±.94
1.55-1.80	0.3±.15	1.0±1.9	1.5±.47
1.80-2.05	0.2±.12	0.0±.48	0.5±.28
2.05-2.30	0.0±.01	0.0±.34	0.0±.16
2.30-2.55	0.0±.00	0.0±.25	0.0±.07
2.55-2.80	0.0±.00	0.0±.23	0.0±.07
2.80-2.90	0.0±.01	0.0±.00	0.0±.07
2.90-3.00	0.2±.16	0.0±.17	0.1±.10
3.00-3.10	0.2±.17	0.0±.06	0.2±.14
3.10-3.20	0.2±.16	0.0±.15	0.2±.14
3.20-3.30	0.0±.00	0.0±.00	0.0±.01
3.30-4.00	0.0±.00	0.0±.05	0.0±.00
4.00-5.00	0.0±.00	0.0±.00	0.0±.00

the most central rapidity interval might be related to the acceptance cutoff and the shift of the peak of the rapidity distribution to lower rapidities as the centrality of the event increases.

The excess of $\mu\mu$/(charged multiplicity) with respect to p–W minimum bias interactions as a function of transverse mass is presented in Fig. 10 for the lower and higher mass continuum intervals, 0.2–0.6 GeV/c^2 and 1.35–2.5 GeV/c^2, respectively. The turnover in the first m_T-bin is due to acceptance cuts. The transverse mass spectrum seems to scale with m_T in yield and shape, with a similar larger excess of low statistical significance at intermediate mass for peripheral collisions. The fitted inverse slope parameter to the low mass m_T distribution gives consistent values for peripheral and central collisions within 12 MeV and the statistical errors of the fit.

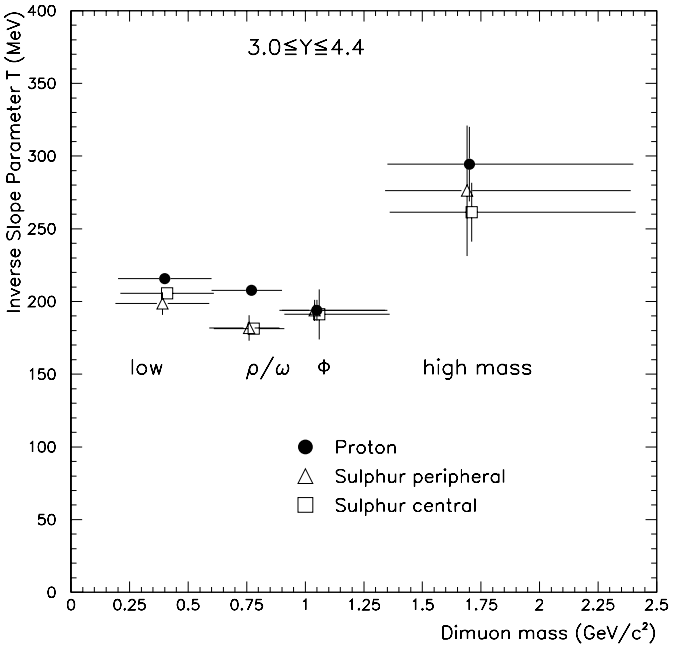

Fig. 7. Inverse slope parameter fitted to transverse mass distributions of different mass regions for p–W minimum bias interactions, S–W peripheral interactions and S–W central interactions

Table 5. The multiplicity-averaged relative excess [(S–W) – (p–W)]/p–W in different mass and rapidity intervals. The low mass values in the forward region are based on central events only

Rapidity	$3.0 \le y \le 3.9$	$3.9 \le y \le 4.4$	$4.4 \le y \le 7.0$
mass (GeV/c^2)			
$0.20 \le M_{\mu\mu} \le 0.6$	0.75 ± 0.07	0.76 ± 0.05	0.26 ± 0.05
$1.35 \le M_{\mu\mu} \le 2.4$	2.8 ± 0.4	1.8 ± 0.3	2.5 ± 0.6

Figure 11 shows the fitted inverse slopes of the transverse mass distributions for the low mass interval vs. multiplicity. It is clear that with the exception of the lowest multiplicity class the fitted slopes are independent of centrality within the errors and have an average inverse slope parameter of $T = 190 \pm 5$ MeV/c^2, typical for m_T spectra of relatively low mass mesons, like the ones plotted in Fig. 6.

Summarizing this comparison of S–W and p–W data, we observe an excess of dimuon pairs in S–W relative to p–W collisions which does not increase with the charged multiplicity. The inverse slope parameters describing the transverse mass distributions of the muon pairs of S–W and p–W collisions are consistent within the errors, with the exception of a small deviation for the ρ/ω resonance.

4.2 The intermediate mass region ($1.35 < m_{\mu\mu} < 2.5$ GeV/c^2)

In Table 6, we give the experimental results for dimuons in the entire kinematic region (rapidities below 7.0) for p–W minimum bias interactions, and for individual classes 3–6 for S–W interactions.

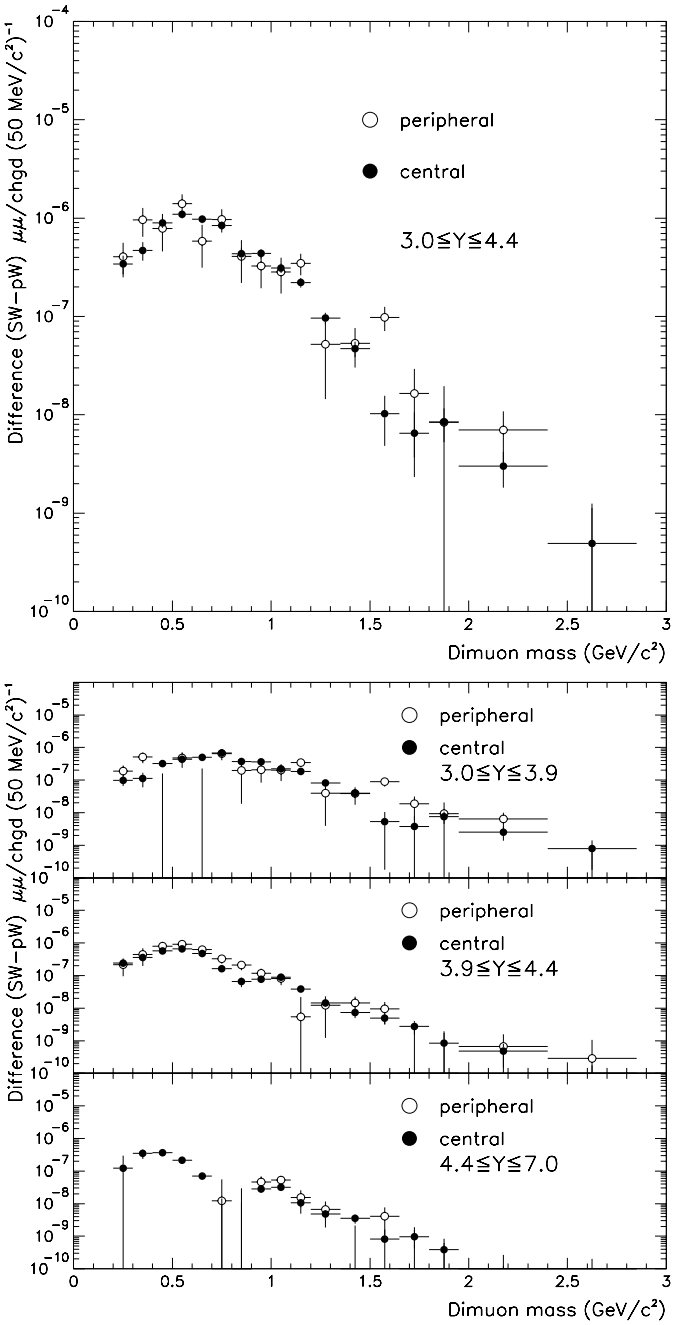

Fig. 8. Excess of $\mu\mu$/(charged multiplicity) between the S–W central and peripheral interactions, and the p–W minimum bias interactions as a function of mass. The excess is defined as the difference between the S–W and p–W ratios at each mass point. The complete rapidity interval 3.0–7.0 is divided in three on the lower figure, omitting the low mass data for peripheral collisions in the most forward rapidity bin

Figure 12 shows the p–W minimum bias dimuon mass spectrum in the whole kinematic region, as well as in individual p_T and y bins, whereas in Fig. 13 the S–W dimuon spectrum is shown for multiplicity classes 3-6 in the whole kinematic region. Estimates of the known dimuon sources

Table 6. The $\mu\mu$/(charged multiplicity) ratio (≡ number of dimuons in the given mass bin integrated over all p_T and normalized to the number of charged particles measured in $3.5 < \eta < 5.2$), as a function of mass for rapidities $y \leq 7$. Note the variable mass bins. The results in the first bin are affected by the dimuon threshold

Mass interval (GeV/c^2)	p–W	S–W class 3	S–W class 4	S–W class 5	S–W class 6
		$10^9 \times (\mu\mu/0.05\ GeV/c^2)$ per charged particle			
0.20-0.25	1268.±217.	1846.±551.	1933.±239.	1189.±177.	1486.±166.
0.25-0.30	2398.±313.	3422.±865.	3131.±343.	2972.±250.	2695.±259.
0.30-0.35	2634.±228.	3116.±653.	3729.±292.	3193.±206.	3305.±244.
0.35-0.40	2254.±168.	4091.±657.	3182.±278.	2986.±199.	2934.±247.
0.40-0.45	1933.±102.	2595.±560.	3592.±263.	2828.±182.	2760.±230.
0.45-0.50	1419.±74.	3785.±564.	2966.±241.	2421.±171.	2538.±226.
0.50-0.55	1269.±70.	2820.±518.	2544.±235.	2381.±167.	2315.±218.
0.55-0.60	1140.±63.	2107.±470.	2565.±222.	2559.±166.	2694.±221.
0.60-0.65	958.±67.	1799.±464.	2125.±201.	1978.±149.	2028.±204.
0.65-0.70	1106.±64.	2181.±420.	2322.±194.	1950.±144.	1759.±185.
0.70-0.75	1413.±56.	2913.±416.	2496.±185.	2154.±139.	2410.±190.
0.75-0.80	1609.±55.	1959.±353.	2165.±167.	2368.±131.	2174.±167.
0.80-0.85	1456.±48.	1639.±278.	2149.±152.	1624.±110.	1980.±152.
0.85-0.90	1081.±41.	1455.±283.	1709.±136.	1142.±92.	1130.±124.
0.90-0.95	716.±34.	1389.±263.	1160.±112.	1205.±90.	917.±112.
0.95-1.00	436.±24.	871.±214.	874.±93.	1009.±79.	975.±99.
1.00-1.05	402.±23.	674.±172.	760.±77.	827.±66.	809.±89.
1.05-1.10	309.±20.	567.±158.	551.±69.	600.±53.	790.±76.
1.10-1.15	200.±16.	593.±133.	523.±60.	490.±46.	448.±63.
1.15-1.20	102.±12.	249.±96.	304.±49.	214.±35.	276.±50.
1.20-1.25	60.6±8.6	125.±80.	128.±40.	143.±31.	163.±42.
1.25-1.40	20.8±2.9	79.4±39.	145.±20.	110.±14.	84.±18.
1.40-1.55	15.2±2.2	47.8±24.	42.6±12.	34.1±8.8	58.7±13.
1.55-1.80	5.9±1.1	45.5±15.	12.0±5.8	17.3±4.6	19.6±6.3
1.80-2.05	3.0±.77	11.9±7.7	10.4±3.6	9.9±2.8	12.8±4.2
2.05-2.30	2.0±.56	9.0±5.8	6.1±2.9	5.4±1.9	2.1±2.3
2.30-2.55	1.0±.31	0.0±2.0	0.7±1.3	2.6±1.2	0.0±1.3
2.55-2.80	1.7±.48	0.7±1.7	2.6±1.4	0.8±.65	2.2±1.2
2.80-2.90	2.3±.73	0.8±1.7	1.6±1.8	5.1±1.6	1.0±1.0
2.90-3.00	8.3±1.8	13.3±5.7	11.1±4.6	5.1±1.4	4.1±1.5
3.00-3.10	20.4±2.6	25.1±12.	12.6±3.0	13.8±2.5	19.7±6.7
3.10-3.20	23.4±3.0	23.5±9.6	8.5±2.6	14.5±3.2	12.7±4.0
3.20-3.30	11.0±2.9	6.8±7.0	4.2±2.5	2.9±1.1	2.7±1.2
3.30-4.00	0.8±.19	0.0±.37	1.3±.53	0.6±.23	0.7±.44
4.00-5.00	0.1±.03	0.0±.00	0.2±.10	0.1±.13	0.0±.01

contributing to the mass region between the ϕ and J/ψ vector mesons are superimposed and will be discussed in the next subsection.

4.2.1 Known contributions

In the mass region $1.35 < m_{\mu\mu} < 2.5\ GeV/c^2$, three sources are expected to contribute to the dimuon continuum:

a) tails of the lower lying vector mesons (ρ, ω, ϕ),
b) simultaneous semileptonic decays of charmed particles,
c) the Drell-Yan process.

In this mass region, the mesons can contribute due to the mass resolution of the apparatus and the ρ, in addition, due to its decay width; nonetheless sources *b*) and *c*) are dominant.

Since none of the aforementioned processes was measured under the same conditions as the HELIOS/3 data (beam, target, energy, kinematic window etc.) it was nec-

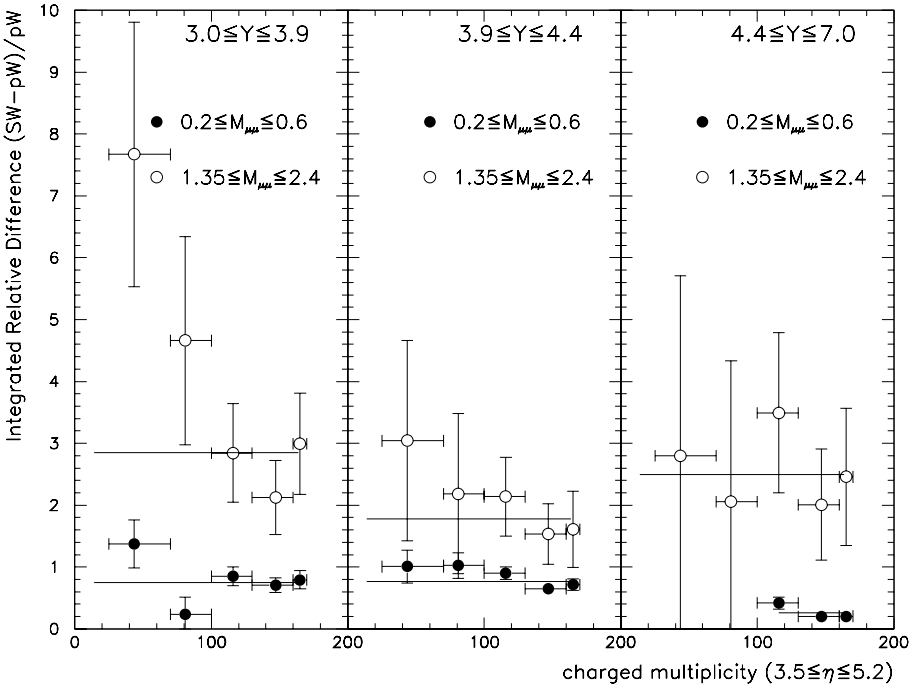

Fig. 9. Significance of the excess of $\mu\mu$/(charged multiplicity) between the S–W interactions and the p–W minimum bias interactions as a function of charged particle multiplicity in S–W interactions for two continuum mass regions. The data are divided into three rapidity intervals. The significance is defined as the difference between the S–W and p–W data integrated over the relevant mass interval, and normalized to p–W. Note that a significance of 1, for example, indicates an excess equal to the p–W contribution

essary to extrapolate all known cross sections and to use Monte Carlo models where no appropriate information was available. Estimations of the different contributions were done as follows:

Mesons: the ρ meson shape in the dimuon mass spectrum was taken as in [37,38]

$$B_\rho(m) = \sigma(m)\frac{\pi^{-1}m^2\Gamma_{\rho\to\mu\mu}(m)}{(m^2-m_\rho^2)^2+m^2\Gamma^2_{\rho\to\pi\pi}(m)} \qquad (4)$$

where

$$\Gamma_{\rho\to\mu\mu}(m) = \frac{k}{k_0}\frac{(2m_\mu^2+m^2)}{(2m_\mu^2+m_\rho^2)}\frac{m_\rho^6}{m^6}\Gamma^0_{\rho\to\mu\mu} \text{ and}$$

$$\Gamma_{\rho\to\pi\pi}(m) = \left(\frac{k}{k_0}\right)^3\left(\frac{m_\rho}{m}\right)^2\Gamma^0_{\rho\to\pi\pi}$$

$$k = \sqrt{0.25m^2-m_\mu^2} \text{ and } k_0 = \sqrt{0.25m_\rho^2-m_\mu^2}$$

and $\sigma(m)$ is the cross section for the production of a particle with mass m (summed over all spin states). Its functional form was found in analogy with the approach used for ρ meson searches in the $\pi\pi$ channel, where it is assumed to behave like the non-resonant background under the meson. Since the spectroscopy of produced hadrons was not possible in HELIOS/3, the QGSM model [39] for p-p interactions at 200 GeV/c was used. We parameterized the uncorrelated $\pi\pi$ phase space spectrum $PS(m)$

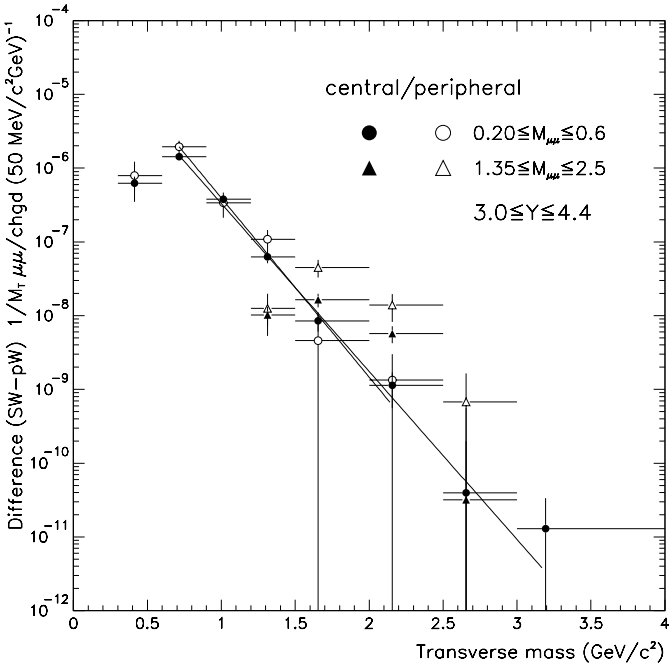

Fig. 10. Excess of $\mu\mu$/(charged multiplicity) between the S–W central and peripheral interactions, and the p–W minimum bias interactions as a function of transverse mass for two continuum mass bins. The excess is defined as the difference between the S–W and p–W ratios at each mass point. The ratio is divided by M_T to obtain an exponential distribution

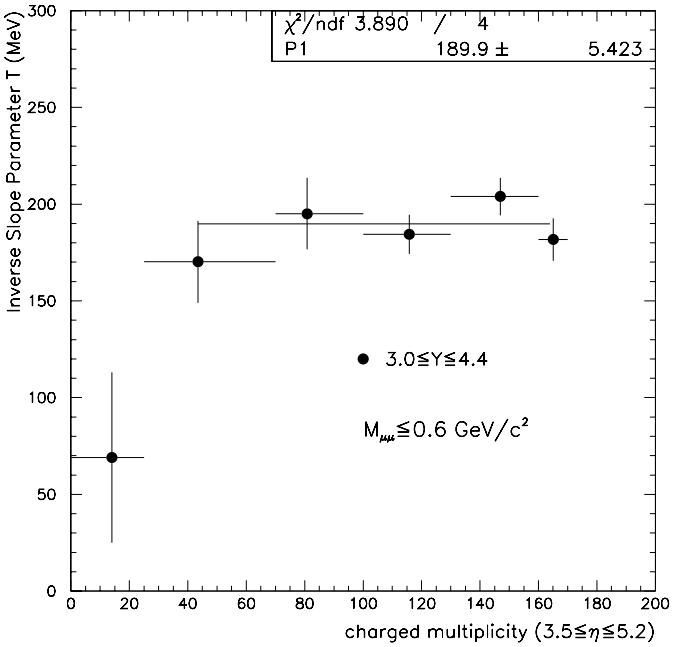

Fig. 11. Fitted inverse transverse mass slope vs. multiplicity for the excess of muon pairs $\mu\mu$/(charged multiplicity) with respect to p–W minimum bias interactions in all S–W multiplicity classes

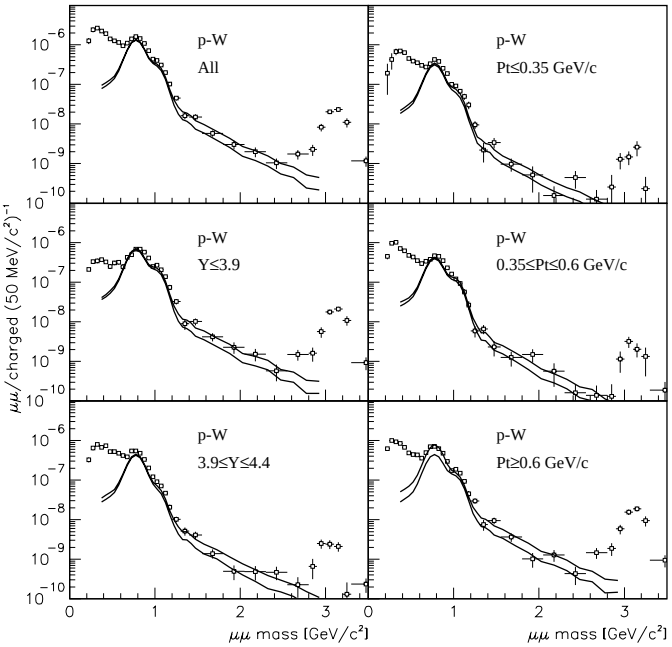

Fig. 12. Measured $\mu^+\mu^-$ mass spectra for different kinematic regions for p–W interactions with superimposed expected sources contributing to the intermediate mass region. The overall systematic error of the calculation is indicated by the band between the two lines. The restricted p_T regions are for all y, and vice versa

as

$$PS(m) = \left(\frac{k_\pi}{m}\right)^\beta \exp(ak_\pi + bk_\pi^2)$$

$$k_\pi = \sqrt{0.25m^2 - m_\pi^2}$$

with $\beta = 0.5725$, $a = -4.5729$ and $b = 0.3130$. In order to define $PS(m)$ also below the $\pi\pi$ threshold mass, the pion mass was replaced with the muon mass. Finally, to avoid counting the phase space of the final state twice (see e.g. [37]), we used

$$\sigma(m) = PS(m)\frac{m}{k_\pi} \tag{5}$$

The cross sections for ρ and ω production were chosen according to the relation $B_\rho\sigma_\rho/B_\omega\sigma_\omega = 0.6$, corresponding to $\sigma_\rho/\sigma_\omega = 1$ as known from p-p experiments [25]. This choice hardly influences the results of this paper.

The ω and ϕ mesons ($\Gamma_\omega^{tot} = 8.41$ MeV/c^2 and Γ_ϕ^{tot} =4.43 MeV/c^2 [40]) are very narrow and in the dimuon mass spectrum they appear as Gaussian peaks with the widths given by the mass resolution (82 MeV/c^2) of the spectrometer. The contributions of the vector mesons were determined by fitting the data in the mass interval $0.3 \leq m \leq 2$ GeV/c^2 by the function

$$F(m) = P_1[0.6B_\rho(m) + G_\omega(m) + P_2G_\phi(m)] + C(m)$$

where G_i were Gaussians describing the ω and ϕ meson peaks, the B_ρ is the rho meson shape described by (4), and

$$C(m) = (P_3e^{P_4m} + \frac{P_5}{m^3}e^{P_6m})(1 - \frac{2m_\mu}{m})^{P_7}$$

represents the continuum parameterization chosen to describe its behavior at threshold and high mass (i.e. Drell-Yan-like) [18]. $P_1 \ldots P_7$ are the parameters determined by the fit.

Semileptonic charm decays: Charm is produced in hadronic collisions mainly via gluon-gluon fusion, which is a hard process and can be treated using perturbative QCD. The mass spectrum of the muon pairs created in simultaneous decays of the particles with open charm was estimated in the framework of the Pythia 5.6 and Jetset 7.3 models tuned to reproduce the measured $D\bar{D}$ differential distributions [41]. $pp \to c\bar{c}$ events at 200 GeV/c were generated and the muon pairs were processed through the spectrometer response simulation using the Geant Monte Carlo program. All dimuons processed by Geant were reconstructed in the same way as the data. Although the dimuon decay angular distribution depends on the dimuon mass, varying from an approximate isotropy at masses around 1 GeV/c^2 to forward–backward peaking at higher masses [19], this procedure correctly mimics our data analysis.

The experiments measuring charm production in interactions of protons with nuclear targets are somewhat contradictory with respect to the A dependence of the cross sections, some experiments being compatible with an A^α dependence with $\alpha = 2/3$ and others with $\alpha \approx 1$ [42]. But recent experiments utilizing precise vertex detectors for the detection of the charm decays [43,44] report results compatible with $\alpha = 1$. No experiment reported $\alpha > 1$.

Therefore we assumed a linear A dependence expected for hard processes.

For the prediction of the dimuon contribution from charm decays in p–W and S–W interactions, the cross section per nucleon-nucleon collision obtained from the indirect measurement performed by the NA38 collaboration [23] in p–W collisions at 200 GeV/c was used. They reported the value $\sigma^{c\bar{c}} = (9.5 \pm 2.0)\mu b$/nucleon.

One must notice the higher value of $\sigma^{c\bar{c}}$ obtained by this indirect method compared to the cross section from direct charm measurements by NA25 and NA32 [41,45]. However, the indirect measurement uses the Pythia model which underestimates $D^{\pm}$ yield relative to D^0, while describing the charm meson correlations, relevant for the shape of the dimuon mass spectrum from semileptonic decays, quite well (for details see [46]). Taking into account the fact that the branching ratio $BR(D^{\pm} \to eX) = (17.2\pm1.9)\%$ is larger than $BR(D^0 \to eX) = (6.75\pm0.29)\%$ ($\mu X = (6.6\pm0.8)\%$) [40], it is not surprising that one needs systematically larger charm production cross section to match the dilepton yield with Pythia predictions.

Since our estimation of the dimuon yield from semileptonic charm decays starts with the NA38 cross section, determined by an adjustment of their data to the Pythia predictions, we remove systematic errors of this model to a large extent.

In order to take into account the variations of the indirectly obtained value of $\sigma(c\bar{c})$ which depends on various inputs used in the NA38 analysis, we added a 30% systematic error to our predictions (this makes our choice consistent also with the more recent value of $6.4\mu b$/nucleon reported in [47]).

Drell-Yan process: the differential cross section and mass spectrum of the lepton pairs produced in the annihilation of the quarks and anti-quarks from the projectile and target nucleons (or nuclei), a hard process, can be calculated using perturbative QCD [48,49]

$$\frac{d^2\sigma}{dm^2 dx_F} = \left(\frac{4\pi\alpha^2}{9m^4}\right)\frac{1}{x_1+x_2}\times \sum_{q=u,d,s} e_q^2\left(f_q^P(x_1)f_{\bar{q}}^T(x_2) + f_{\bar{q}}^P(x_1)f_q^T(x_2)\right) \quad (6)$$

$$x_1 = \frac{1}{2}\left(\sqrt{x_F^2+4\tau} + x_F\right)$$

$$x_2 = \frac{1}{2}\left(\sqrt{x_F^2+4\tau} - x_F\right)$$

P and T denote the projectile and target, respectively, e_q is the quark electric charge, α the fine structure constant, x_1 and x_2 are the fractions of the projectile and target momenta, respectively, carried by colliding partons, $x_F = x_1 - x_2$ is the Feynman variable calculated in the center of mass system and $\tau = m^2/s = x_1x_2$. Our data in the kinematic window (1) are sensitive to $x_1 \approx 0.06 - 0.9$ and $x_2 \approx 0.003-0.2$. The structure functions $f_q(x)$ are the same as those measured in deep inelastic scattering (DIS). This formula, sometimes referred to as the "naïve Drell–Yan model", says nothing about the dilepton transverse momentum distribution which in Monte Carlo models like Pythia is mostly generated via the intrinsic parton momenta inside hadrons.

The expression (6) for the cross section has to be multiplied by a K-factor ≈ 2, i.e.

$$\sigma_{DY}^{experiment} = K\sigma_{DY}^{naive}$$

to take into account higher order graphs in perturbative QCD. The value of K is almost independent of the incident particles, $\sqrt{s}$ and dilepton mass [48,49]. Since our data sample did not contain sufficient dimuons with masses above the J/Ψ meson, it was impossible for us to obtain the K value directly from our experiment. We chose the value $K = 2.5\pm0.5$ based on previous dimuon experiments [50], where the error bar reflects our uncertainty. Comparison of the different structure function sets from Pdflib [51] showed 20% variations of the cross section predictions, caused by the differences in the parameterizations of the sea quark distributions at small x.

Measurements of the Drell-Yan production in the collisions of hadrons with nuclear targets showed a linear A dependence of the cross section. Since our data samples were taken with a heavy target, we investigated also the influence of the changes in the parton distributions in the nuclear medium known from DIS experiments [52]. These measurements revealed that the nuclear medium affects mostly the sea quark/anti-quark distributions at small x. According to our rough estimations, a similar decrease of the cross sections of about 25% could be expected in the p–W and S–W collisions, almost independent of the selected kinematic subregion (2).

Since the effect was found to be of a similar magnitude as the uncertainty coming from different structure function parameterizations and no important changes in the calculated dimuon mass distributions were found, it was decided to fix the cross section (per nucleon-nucleon collision) by selecting the set which leads to the best description of the p–W data without including any scheme for the description of nuclear effects in the analysis [19]. In our case it was the Morfin-Tung set 1 ($\overline{MS}$) [53]. We obtained the following cross sections integrated over $-1 \le x_F \le 1$ and $1 \le m_{\mu\mu} \le 4$ GeV/c^2: $\sigma_{DY}^{pW} = K \times 4.7$ nb/nucleon and $\sigma_{DY}^{SW} = K \times 4.3$ nb/nucleon for p–W and S–W collisions, respectively. A 30% systematic error reflecting the theoretical uncertainties was added to the predictions.

The shape of the mass spectrum produced in the process of the quark-antiquark annihilation and the fraction of the phase space corresponding to the kinematic region (1) was estimated using Pythia 5.6 with the Morfin-Tung set 1 structure functions, taking into account the nuclear composition (see [51,53,54]). The slope of the intrinsic parton transverse momentum distribution was tuned, so that the mean value of the generated dimuon p_T was 0.8 GeV/c which is close to the experimentally observed value [48]. All generated pairs were further processed by the Geant simulation of the detector and reconstructed in the same way as the data.

4.2.2 Normalization of predictions

Since our data are presented as $\mu\mu/charged$ the predictions were normalized in the same way. The A dependence for the Drell-Yan and charm production processes was expressed as:

$$\left(\frac{\mu\mu}{charged}\right)_i^P = \frac{\tilde{A}\sigma_{KR}^P}{\sigma_{inel}F_i\langle n_{charged}\rangle} \tag{7}$$

where P denotes the Drell-Yan or charm production process, i the multiplicity class, σ_{KR}^P is the cross section of a given process in the kinematic window (1) or (2), σ_{inel} is the inelastic cross section in p–W or S–W collisions, F_i is the fraction of the inelastic cross section corresponding to the given multiplicity class i, and $\langle n_{charged}\rangle$ is the mean charged particle multiplicity. $\tilde{A}$ is $A_W = 184$ for p–W collisions and

$$\tilde{A} = \int T_{SW}(\mathbf{b}) w_i(b) d^2\mathbf{b} \tag{8}$$

for S–W collisions where $T_{SW}(\mathbf{b})$ is the thickness function normalized by

$$\int T_{SW}(\mathbf{b}) d^2\mathbf{b} = A_S A_W$$

and $w_i(b)$ is the probability that an inelastic event produced at the impact parameter b fulfills the trigger criteria for i-th multiplicity class. We can only estimate the $w_i(b)$ functions using a physics generator. After comparisons of the predictions of various models with the experimental charged particle multiplicity distributions [55], we decided to use for this analysis the DTUNUC 1.02 model [29] which gave the most satisfactory results (more details are given in [19]). The fractions F_i are estimated with the same model, using the impact parameters for each class.

The p–W and S–W inelastic cross sections were calculated using the procedure described in [28]. The cross sections obtained in that way were $\sigma_{inel}^{pW} = (1634 \pm 10 \pm 37)\ mb$ for p–W collisions and $\sigma_{inel}^{SW} = (3872 \pm 28 \pm 68)\ mb$ for S–W collisions. The first error reflects the uncertainty of the nucleon-nucleon inelastic cross section and the second error is our estimation due to the uncertainties of the nuclear density parameterization.

4.2.3 Error Analysis

The contributions to the error of (7), later shown as bands on the figures, are:

- measurement errors of the charm production cross section,
- uncertainty of K-factor for the Drell-Yan process,
- uncertainty due to different structure function sets,
- estimated systematic errors for Drell-Yan and charm production,
- uncertainties of the calculation of the inelastic p–W and S–W cross sections,

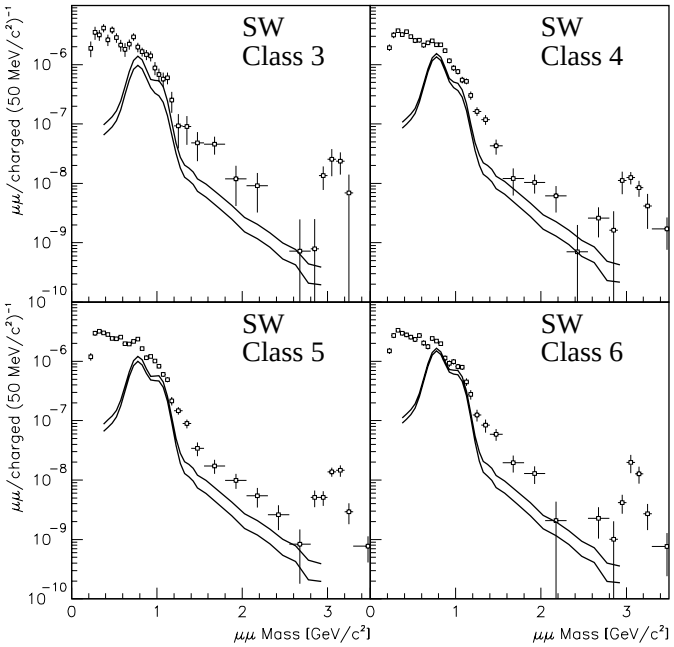

Fig. 13. Measured $\mu^+\mu^-$ mass spectra for different S–W multiplicity classes with superimposed expected sources contributing to the intermediate mass region

- uncertainties of the ρ, ω and ϕ contributions obtained by fitting the measured dimuon spectra,
- uncertainty of $n_{charged}$,
- estimated uncertainties of $\tilde{A}$ and F.

The relative errors of the predicted yield from the known sources for the mass region 1.35 - 2.5 GeV/c^2 for p–W (S–W minimum bias class) are about 41% (41%) for the Drell-Yan contribution, about 36% (36%) for charm production, about 6×10^{-4} (3×10^{-3}) for ρ production and about 9×10^{-6} (4.9×10^{-5}) for the ϕ production. The choice of a different mass region will result in somewhat different error contributions, reflecting the differences in the relative composition of the sources under consideration. The total relative error for the predicted sources is about 30% dominated by uncertainties for predicted yields from Drell-Yan and charm production.

4.2.4 Comparison with known sources

Figure 12 shows the measured p–W dimuon mass spectrum in different kinematic windows with the three contributing sources superimposed; no fit or adjustment was performed. Since one does not expect a new source in this sample, the comparison can serve as a "measure" of the correctness of the underlying assumptions, in particular for the different p_T and y kinematic regions.

The same operations were performed with S–W data; see Fig. 13 for the results in different multiplicity classes. The expected sources do not describe the S–W measured dimuon mass spectra in the intermediate mass region, and the presence of an additional source of dimuons is clearly visible.

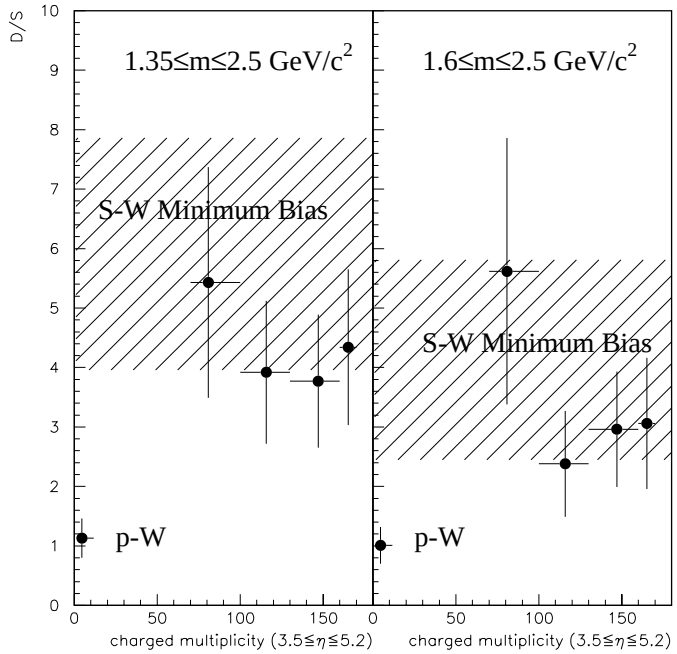

Fig. 14. The excess defined as the integral of the data divided by the integral of the expected dimuon sources as a function of the charged multiplicity in the pseudorapidity interval between 3.5 and 5.2. The shaded area corresponds to 5.91±1.95 and 4.13±1.68

As a quantitative measure of the observed "excess" we use for this analysis the ratio

$$\frac{D}{S} = \frac{\text{Integral contents of data histogram}}{\text{Integral sum of predicted sources}} \qquad (9)$$

which corresponds to the definition of the excess used in Sect. 4.1 and in Fig. 9 shifted by +1.

We evaluated the D/S ratio in two mass intervals:

- interval I: $1.35 < m < 2.5\ GeV/c^2$
- interval II: $1.6 < m < 2.5\ GeV/c^2$

Relative errors for the mass interval I for p–W (S–W minimum bias) are about 30% (30%) for the predicted sources and about 10–20% (20–40%) for our data. The error of D/S contains these errors added in quadrature. It can be seen that the error in p–W data is slightly dominated by uncertainties in predicted contributions, while in S–W data the errors for predicted yields and fluctuations in data are comparable.

The results for the p–W and S–W collisions of the minimum bias class in the kinematic window (1) as well as in all subregions (2) are summarized in Table 7. A similar level of excess in S–W interactions is seen in all kinematic regions, as well as in all multiplicity classes, Fig. 14.

The minimum bias results are the least dependent on the Monte Carlo model used for the estimation of the $w_i(b)$ functions (8) [19]. Therefore the systematic uncertainties of the predictions in this class are reduced.

The D/S dependence on the centrality of the S–W collisions is summarized in Table 8.

5 Discussion and conclusions

Our analysis consists of two different approaches: (1) a direct experimental comparison between the S–W and p–W results for the ratio $\mu\mu$/charged particles and (2) a comparison of the results above the ϕ meson with the expected sources.

For the first approach, the conclusions are summarized as follows:

1. There is a clear excess in $\mu\mu$ production relative to charged particle production in S–W interactions compared to p–W interactions as a function of mass from the $2m_\mu$ threshold to the J/Ψ mass. The excess is defined as the difference between S–W and p–W spectra. This excess presents no apparent resonance structure (*cf.* Fig. 8) and is greater for the intermediate mass region when normalized to the p–W dimuon spectrum. (*cf.* Fig. 9).
2. The excess appears to be unchanged over a wide range of rapidity and does not increase with multiplicity (*cf.* Fig. 9).
3. The inverse slopes of the dimuon transverse mass distributions in S–W and p–W interactions are consistent within 10%, the only exception being the ρ/ω resonance region which appears steeper in S–W collisions (*cf.* Fig. 7).
4. The inverse slope parameter for the transverse mass distribution of low mass excess dimuon pairs appears to be independent of centrality after an onset at low multiplicity (*cf.* Fig. 11).

The numerical results for this approach depend obviously on the acceptance corrections. As already stated in Sect. 3.1, these were obtained by assuming that the decay angular distribution of the dimuon was isotropic. For the low mass region, this is an adequate representation at least for the standard sources [25]. In the intermediate mass region, the two additional sources, Drell-Yan and charm decays, have different decay angular distributions. The former source has a $1 + cos^2\theta$ distribution while the latter varies from approximate isotropy at a dimuon mass = 1 GeV/c^2 to strongly forward-backward peaking at 2.5 GeV/c^2 [19]. We obtain an estimate of the correction that is necessary from the studies in reference [19]. There is essentially no correction (at the few percent level) for the Drell-Yan source while the correction for charm decays increases as the dimuon mass increases beyond 1 GeV/c^2. We have estimated this correction to the standard sources as $R(m) = 1 + \delta R$ with δR changing from zero to 1.5 for the mass region from 1.0 to about 2.5 GeV/c^2 with a 25% error on δR. We do not know if this correction is to be applied to the source responsible for the excess since its decay distribution is not known. *Care should be taken with respect to the decay angular distribution of the new source of dimuons in models which attempt to explain the excess.*

We also caution the reader that this approach is not easy to interpret without a model in that the fixed rapidity intervals for the $\mu\mu$ selection and the fixed pseudo-rapidity intervals for the charged particle selection do not sample exactly the same part of phase space for S–W and p–W in-

Table 7. D/S values in various kinematic subregions for p–W and S–W minimum bias interactions. (Dimuon transverse momentum p_T in GeV/c)

	p–W		S–W minimum bias	
Mass Interval	I	II	I	II
GeV/c^2	$1.35 < m < 2.5$	$1.6 < m < 2.5$	$1.35 < m < 2.5$	$1.6 < m < 2.5$
Whole kinematic region equation (1)	1.13 ± 0.33	1.01 ± 0.31	5.91 ± 1.95	4.13 ± 1.68
$y < 3.9$, all p_T	1.25 ± 0.37	1.17 ± 0.37	7.65 ± 2.63	5.30 ± 2.29
$3.9 < y < 4.4$, all p_T	1.20 ± 0.39	0.96 ± 0.35	3.08 ± 1.33	2.38 ± 1.35
$p_T < 0.35$, all y	1.13 ± 0.37	0.98 ± 0.38	3.68 ± 1.87	1.80 ± 1.21
$0.35 < p_T < 0.60$, all y	1.21 ± 0.38	1.20 ± 0.44	3.84 ± 1.56	3.30 ± 1.48
$p_T > 0.60$, all y	1.10 ± 0.34	0.93 ± 0.31	7.37 ± 2.68	5.07 ± 2.46

teractions. However, the differences are somewhat reduced in the double ratio, $\mu\mu$/charged.

The second approach does not have these difficulties, but it involves the comparison to models of Drell-Yan and charm production. However, no arbitrary parameters are fitted. The conclusions are summarized as follows:

5. The shape and absolute value of the dimuon signal in the mass range between ϕ and J/Ψ masses, observed in the kinematic windows (1) and (2) in p–W interactions at 200 GeV/c (*cf.* Table 7), is described using only three sources:
   a) tail of the mass spectra of the ρ, ω and ϕ mesons,
   b) semileptonic decays of charmed particles,
   c) Drell-Yan process.
6. The extrapolation of these three contributions to central S–W interactions cannot describe the observed signal (*cf.* Table 8).
7. Quantitatively, the D/S value defined by (9) found in p–W data is compatible with one. For S–W data, D/S differs from unity by about 3σ for each of the four multiplicity classes considered, and is also about 3σ for the minimum bias class (*cf.* Table 7-8, Fig. 15).
8. The comparison of the D/S values for the S–W minimum bias in the kinematic region (1) with those in the four central S–W classes shows no significant change of the observed excess as a function of collision centrality (*cf.* Table 8, Fig. 14).

It should be noted that a weaker A dependence of charm production in hadronic interactions as measured in some experiments would increase the observed excess. No experiment has reported an A^α dependence with $\alpha > 1$.

For the intermediate mass region, the evaluation of an excess by normalizing the data to the expected contributions from Drell-Yan, open charm and the tail of the meson-resonances, i.e. D/S, gives quantitatively compatible results with the direct comparison between p–W and S–W data as performed in the first part of the analysis.

The NA38/50 collaboration has presented a similar analysis giving a value $D/S = 1.26 \pm 0.1$ for the mass range of $1.5 < M_{\mu\mu} < 2.5$ [23]. This result is in qualitative agreement with our measurement. They also found a negligible multiplicity dependence of the observed excess. Since their data are not corrected for the acceptance which decreases rapidly for masses below 2.5 GeV/c^2, the quantitative comparison has to be judged with care. In a more recent paper[56] the same authors discuss the observed excess of dimuon pairs in terms of an abnormally enhanced open charm component and claim an increase of the enhancement factor with centrality.

Table 8. D/S values in different S–W multiplicity classes in the HELIOS/3 dimuon kinematic region

	S–W collisions	
Multiplicity	Interval I (GeV/c^2)	Interval II (GeV/c^2)
class	$1.35 < m < 2.5$	$1.6 < m < 2.5$
3	5.43 ± 1.94	5.62 ± 2.24
4	3.92 ± 1.20	2.38 ± 0.89
5	3.77 ± 1.12	2.96 ± 0.97
6	4.34 ± 1.31	3.06 ± 1.10

An excess of lepton pairs has also been reported in the low mass region by the CERES collaboration, but with lower statistics and worse signal to background ratio. The ϕ and ρ–ω are at best poorly resolved from the continuum in S–Au interactions [24]. The excess in S-Au interactions is determined by a comparison with all known hadronic sources. The ratio of the data to the sources integrated from 0.2 to 1.5 GeV/c^2 is 5.0±0.7(stat)±2.0(syst).

Since the excess reported in this paper spans in a smooth fashion the low and intermediate mass regions, it seems economical to seek a unique origin. Studies based on a quark-gluon phase transition followed by a mixed phase and a hadronic gas [57–59], or on open charm production [46] cannot account for the excess dimuons easily. As discussed in [15,36] the shape of the data (HELIOS-3 and CERES) cannot be reproduced in the low mass region by such a scenario. A different contribution, π–π annihilation, leads to a pronounced peak in the dilepton mass spectrum around the ρ resonance but falls below the data around 400 MeV/c^2.

It has been proposed [59–61] that π–π and other meson–meson annihilation processes are enhanced by the achieved high particle densities and can account for at

least the low mass part, if the ρ effective mass and width change due to in-medium effects. Such models can reproduce the low mass region [15,36] as well as the mass spectrum above the ϕ-resonance [16,17]. On the other hand, attempts to interpret the enhancement of lepton pairs in terms of many-body effects also yield good agreement with the low mass data [62,63]. For a recent discussion see [64].

It has to be seen which scenarios reproduce all data over the entire kinematic region, low and intermediate masses including the observed transverse mass distributions and the (in)dependence on rapidity from central to forward (3.0–7.0).

The scenarios which reproduce the mass and m_T distributions must also be consistent with the measured multiplicity dependences. For example, lepton pair production from a QGP or a hadronic gas via π–π annihilation should have approximately a squared-multiplicity dependence as it relies on the combinatorics of the elementary constituents.

The CERES collaboration has published [65] their electron pair data in a central rapidity interval for Pb-Au collisions: they claim an indication for a stronger than linear dependence on the charged multiplicity. However, it is interesting to note that on average the number of lepton pairs produced per charged multiplicity is similar in S–Au and Pb–Au collisions [24,65] despite the different multiplicities of the two reactions.

A claim for a stronger than linear dependence on the charged multiplicity is deduced in [36] from the analysis of different rapidity bins of our data. However, as explained in Sect. 3.1, the lower limit of transverse mass varies strongly with rapidity and must be treated with care. The effect of the acceptance cuts is demonstrated in Fig. s 8 and 9 where data are compared for three rapidity intervals.

In contrast, the data presented in this paper on the excess of dimuon pairs give no indication for a stronger than linear multiplicity dependence. In the rapidity interval of this experiment, the observed multiplicity dependence is linear (*cf.* Figs. 14 and 9). The relative importance of the underlying physics processes can vary over the accepted kinematic region. We emphasize that the dependence on multiplicity is an important indicator of these processes and could be used to distinguish theoretical models in dilepton production.

Acknowledgements. The HELIOS/3 collaboration wishes to thank the staff of the PS-SPS accelerator complex for their outstanding performance. The valuable contributions of the technical staff of CERN and the collaborating institutes are gratefully acknowledged. We are grateful for support by the Direction des Sciences de la Matière (CEA, France), the Istituto Nazionale di Fisica Nucleare of Italy and the Natural Sciences and Engineering Research Council of Canada.

References

1. K. Kajantie, J. Kapusta, L. McLerran and A. Mekjian, Phys. Rev. D **34**(1986)2746.
2. P. V. Ruuskanen, Nucl.Phys. A **525** (1991) 255c.
3. P. V. Ruuskanen in "Proceedings of the LHC Workshop", Vol.II, (1991) CERN 90-10, 1164.
4. C. A. Dominguez and M. Loewe, Z.Phys. C **49** (1991) 423.
5. P. V. Ruuskanen Nucl.Phys. A **544** (1992) 169.
6. J.Alam et al. Nucl.Phys. A **544** (1992) 493c.
7. J. Masarik, N. Pišútová and J. Pišút, Z. Phys C **59** (1993) 285 and J. Masarik, N. Pišútová and J. Pišút, Z. Phys C **62** (1993) 499.
8. A. V. Leonidov and P. V. Ruuskanen, Eur. Phys. J. C **9** (1998) 519.
9. P. Koch, Z.Phys. C **57** (1993) 283.
10. B. Kämpfer, P. Koch, and O. P. Pavlenko, Phys.Rev. C **49** (1994) 1132.
11. J. Cleymanns, K. Redlich, and H. Satz, Z.Phys. C **52** (1991) 517.
12. R. D. Pisarski, Phys.Lett. B **110** (1982) 155.
13. G. E. Brown and M. Rho, Phys.Reports. **269** (1996) 333.
14. T. Hatsuda and S.-H. Lee, Phys.Rev. C **46** (1992) 34.
15. B. Friman, Nucl.Phys. A **610** (1996) 358c, and many references therein.
16. G. Q. Li and C. Gale, 13th International Conference on Ultra-relativistic Nucleus-nucleus Collisions: Quark Matter '97 Tsukuba, Japan ; 1 - 5 Dec 1997; Nucl.Phys. A **638**, (1998) 491c.
17. G. Q. Li et al. APCTP Workshop on Astro-Hadron Physics, Seoul Korea, Oct. 1997.
18. A .L. S. Angelis et al., Eur. Phys. J. C **5** (1998) 63.
19. more details are to be found in I. Kralik, Intermediate Mass Dimuon Production in p–W and S–W Collisions at 200 GeV/c/A, PhD Thesis, Inst. of Experimental Physics, Košice, 1995, unpublished.
20. J. Antos, Perturbative QCD and Hadronic Interactions, ed. J. Tran Thanh Van, Editions Frontieres (1992) 485.
21. U. Goerlach (HELIOS/3 coll.), Sixth "Rencontres de Blois", Château de Blois, France, ed. J. Tran Thanh Van, Editions Frontieres (1994) 525.
22. M. Masera (HELIOS/3 coll.), Nucl.Phys. A **590**, (1995) 93c.
23. C. Lourenço et al. (NA38 Collaboration), Nucl. Phys. A **566** (1994) 77c; C. Lourenço et al. (NA38 Collaboration), Hirschegg, Austria (1995), CERN-PPE/95-72; A. E. Scomparin, (NA38 Collaboration) Nucl. Phys. A **610** (1996) 331c.
24. G. Agakichiev et al., (CERES Coll.), Phys. Rev. Lett. **75** (1995) 1272.
25. T. Åkesson et al., Z. Phys. C **68** (1995) 47.
26. M. Masera, 24*th* Rencontres de Moriond, New results in hadronic interactions, J. Tran Thanh Van editor, Editions Frontieres (1989) 477
27. K. Werner, Phys. Rev. Lett. **62** (1989) 2460.
28. K. Werner, Phys. Rep. **232** (1993) 87.

29. J. Ranft, SSC-report **150** (1987), H.-J. Möhring, J.Ranft, Z. Phys. **C52** (1991) 643 and I. Kawrakow, H.-J. Möhring, J.Ranft, Z. Phys. C **56** (1992) 115.
30. B. Andersson, G. Gustafsson and B. Nilsson-Almqvist, Nucl. Phys. B **281** (1987) 289.
31. M.-A. Mazzoni, HELIOS/3 note 50.
32. J. Bystricky et al., HELIOS/3 note 82, to be submitted to NIM.
33. G. London, HELIOS/3 note 93.
34. G. G. Henry, Ph.D. Thesis, University of Chicago (1978) K. J. Anderson et al., Phys. Rev. Lett. **37** (1976) 799.
35. G. Baroni et al., Nucl. Phys A **531** (1991) 691.
36. A. Drees, Nucl. Phys A **610** (1996) 536c.
37. J. D. Jackson, Il Nuovo Cimento **34** (1964) 1644.
38. Z. Y. Fang, G. Lopez Castro and J. Pestieau, Nuovo Cimento **100A** (1998) 155.
39. N. S. Amelin, K. K. Gudima and V. D. Toneev, NATO ASI series B: Physics **2116** (1989) 473, and preprint GSI 89-52.
40. C. Caso et al., Review of Particle Properties, Particle Data Group, Eur. Phys. J C3 (1998) 1.
41. O. Enriquez et al., Physica Scripta **33** (1986) 202. Phys. Rev. D **50**(1994) 1173.
42. H. Nowak, Fortschritte der Physik **39**(1991) 347.
43. P. Coteus et al., Phys. Rev. Lett. **59**(1987)1530.
44. M. Adamovich et al., Phys. Lett. B **284** (1992) 453.
45. S. Barlag et al., Z. Phys. C **39** (1988) 451.
46. P. Braun-Munzinger et al., Eur. Phys. J. C **1** (1998) 123.
47. A. de Falco et al., Nucl. Phys. A **638** (1998) 487c.
48. I. R. Kenyon, Rep. Prog. Phys. **45** (1982) 1261.
49. K. Freudenreich, Int. J. Mod. Phys. A **5** (1990) 3643.
50. B. Cox, Dimuon Production in Hadronic Interactions, Rapporteur talk at XXI International Conference on High Energy Physics, Paris, 26-31 July 1982, preprint FERMILAB-Conf-**82/69**-EXP, October 1982, and references therein.
51. H. Plothow-Besch, PDFLIB: a Library of All Available Parton Density Functions of the Nucleon, the Pion and the Photon and the corresponding $\alpha(s)$ calculations, Comp. Phys. Comm. **75**(1993) 396, H. Plothow-Besch, PDFLIB: Nucleon, Pion and Photon Parton Density Functions and $\alpha(s)$ Calculations, Int. J. Mod. Phys. A **10** (1995) 2901.
52. M.Arneodo, Phys. Rep. **240** (1994) 301.
53. J. G. Morfin and W.-K. Tung, Z. Phys. C **52** (1991) 13.
54. T. Sjöstrand, Comp. Phys. Comm. **82** (1994) 74 and T. Sjöstrand, CERN-TH.7112/93, (1993), revised August 1994.
55. T. Åkesson et al., Nucl. Phys. B **333** (1990) 48.
56. E. Scomparin et al. (NA50 Coll.), J. Phys. G25 (1999) 235.
57. D. K. Srivastava et al., Phys.Rev. **53** (1996) R567; D. K. Srivastava et al., Nucl.Phys. A **610** (1996) 350c.
58. J. Sollfrank et al., Phys. Rev. C55 (1997) 392-410.
59. G. Q. Li et al., Phys. Rev. Lett. **75** (1995) 4007 and W. Cassing et al., Phys. Lett. B **363** (1995) 35;
60. C. M. Ko et al., Nucl.Phys. A **610** (1996) 342c.
61. W. Cassing et al., Phys. Lett. B **377** (1996) 5.
62. W. Cassing et al., Phys. Rev. C **57** (1998) 916.
63. R. Rapp et al., Phys. Rev. Lett. **76** (1996) 368, Nucl.Phys. A **617** (1997) 472.
64. B. Friman, Talk given at the Joint Session of 97 Korean Physical Society Meeting and APCTP Workshop on Astro-Hadron Physics: Seoul,Korea; 25–31 Oct 1997; nucl-th/9801053, GSI-9807.
65. G. Agakichiev, CERES/NA45 Collaboration, Phys. Lett. B **422** (1998) 405.